The Elastic Stiffness C_{13} in Transversely Isotropic Shales

Colin M. Sayers

Department of Earth and Atmospheric Sciences

University of Houston

cmsayers@central.uh.edu

Version: 2nd September 2026

The Elastic Stiffness C_{13} in Transversely Isotropic Shales

Colin M. Sayers[1]

[1]Department of Earth and Atmospheric Sciences, University of Houston, Houston, Texas 77204-5007, USA

September 2, 2026

Abstract

Shales are often anisotropic due to fine-scale layering and preferred alignment of clay particles with bedding. They may be approximated as transversely isotropic (TI) media with symmetry axis (x_3) perpendicular to bedding. TI media have five independent elastic stiffnesses C_{11}, C_{33}, C_{55}, C_{66} and C_{13}, with $C_{12} = C_{11} - 2C_{66}$. While C_{11}, C_{33}, C_{55} and C_{66} may be estimated from velocities measured parallel and perpendicular to x_3, C_{13} requires measurements at oblique angles, resulting in greater uncertainty. Despite this, C_{13} is important in seismic velocity analysis, imaging, amplitude variation with offset (AVO), and geomechanical applications including wellbore stability, stress estimation, hydraulic fracture design, and reservoir compaction. In isotropic media $C_{13} = C_{33} - 2C_{55}$ and $C_{13} = C_{12}$, but shale microstructure may break these equalities due to preferred orientation of clay particles, fine-scale layering, and bedding-parallel microcracks. For a TI orientation distribution (ODF) of clay particles, the elastic properties may be characterized by two coefficients W_{200} and W_{400} in an expansion of the ODF in generalized Legendre functions. C_{13} may be greater than C_{12} if W_{200} is significantly larger than W_{400}, whereas C_{13} may be lower than $C_{33} - 2C_{55}$ if W_{200} is significantly smaller than W_{400}. Fine-scale layering also influences C_{13}. Depending on layer properties, sequences with $C_{12} < C_{13} < C_{33} - 2C_{55}$ may occur. Bedding-parallel microcracks typically increase $C_{12} - C_{13}$ and $C_{13} - C_{33} + 2C_{55}$, but $C_{13} - C_{33} + 2C_{55}$ may decrease if the ratio of normal-to-shear crack compliance is small, as expected for isolated fluid-filled cracks. These observations provide insight into the physical controls on C_{13} and improve understanding of its variability in shale formations.

1 Introduction

Shales are a major component of sedimentary basins and are anisotropic because of fine-scale layering and partial alignment of anisotropic clay minerals with bedding. To a good approximation, many shales may be considered as transversely isotropic (TI) with axis of rotational symmetry perpendicular to bedding. With axis of rotational symmetry taken as coordinate axis x_3, a TI medium has five independent elastic stiffness coefficients C_{11}, C_{33}, C_{55}, C_{66} and C_{13}, and the elastic anisotropy may be quantified by the three anisotropy parameters ϵ, γ and δ of Thomsen (1986). These parameters are defined in terms of the C_{ij} as follows:

$$\epsilon = \frac{C_{11} - C_{33}}{2C_{33}}, \ \gamma = \frac{C_{66} - C_{55}}{2C_{55}}, \ \delta = \frac{(C_{13} + C_{33})(C_{13} + 2C_{55} - C_{33})}{2C_{33}(C_{33} - C_{55})}. \tag{1}$$

Thomsen's anisotropy parameter δ is seen to depend on C_{13} in addition to C_{33} and C_{55}.

While C_{11}, C_{33}, C_{55} and C_{66} may be determined from measurements of the velocity of P- and S-waves propagating at angles $0°$ and $90°$ to the axis of rotational symmetry, C_{13} can only be obtained by combining velocities measured for propagation parallel and perpendicular to the axis of rotational symmetry with velocities measured at other angles. As an example, if elastic stiffness coefficients C_{11}, C_{33} and C_{55} have been determined from velocity measurements parallel and perpendicular to x_3 then an estimate of C_{13} can be obtained given a knowledge of P-phase velocity V_{P45} for a phase angle of $45°$ to the axis of rotational symmetry as follows:

$$C_{13} = -C_{55} + \sqrt{(C_{11} + C_{55} - 2\rho V_{P45}^2)(C_{33} + C_{55} - 2\rho V_{\mathrm{P45}}^2)}, \tag{2}$$

where ρ is the density of the rock.

This is the approach that has been taken in most experimental determinations of C_{13}. As emphasized by Hornby (1994, 1998), however, this procedure "can lead to unacceptable, and unquantifiable, errors in the reconstruction of the critical C_{13} parameter." An additional complication is whether group or phase velocity is measured in directions other than parallel and perpendicular to the axis of rotational symmetry x_3. If group velocity is measured, then this needs to be converted to phase velocity for use in equation 2.

Despite these difficulties, an estimate of C_{13} is needed for seismic velocity analysis and imaging, and in the identification of reservoir fluids using amplitude variation with offset (AVO) analysis of seismic reflection data from reservoirs and overlying formations. In seismic velocity analysis, the variation of two-way traveltime $t(x)$ of P-waves with offset x (the distance between source and receiver) is given by:

$$t^2(x) = t_0^2 + \frac{x^2}{V_{\mathrm{NMO}}^2}, \tag{3}$$

for small offsets. For P-waves V_{NMO} in equation 3 is the Normal Moveout Velocity given, in terms of the vertical P-velocity V_{P0} and the anisotropy parameter δ of Thomsen (1986) by:

$$V_{\mathrm{NMO}} = V_{\mathrm{P0}}\sqrt{1 + 2\delta}. \tag{4}$$

In P-wave AVO analysis δ is the most important anisotropy parameter (Thomsen 1993; Rüger 1997) so that an understanding of C_{13} is needed for the correct identification of reservoir fluids using seismic reflection data.

Shale anisotropy also needs to be accounted for in geomechanical analysis such as assessment of wellbore stability, determination of in-situ stress, hydraulic fracture design, and estimation of reservoir compaction, and stress changes due to injection and depletion. As an example, assuming zero lateral strain, the change in horizontal stress $\Delta\sigma_1$ due to changes in vertical stress $\Delta\sigma_3$ and pore pressure Δp in a TI layer with vertical axis of rotational symmetry x_3 is given by the theory of anisotropic poroelasticity (Amadei et al. 1987; Thiercelin and Plumb 1994) as:

$$\Delta\sigma_1 = \alpha_1 \Delta p + \frac{C_{13}}{C_{33}}(\Delta\sigma_3 - \alpha_3 \Delta p), \tag{5}$$

where α_1 and α_3 are the horizontal and vertical components of the second-rank Biot-Willis tensor (Biot and Willis 1957).

Because C_{13} plays a critical role in the applications discussed above, and because of uncertainties in its determination from surface seismic data, sonic logs, and laboratory ultrasonic measurements, numerous studies have sought either to estimate C_{13} or to constrain its possible range in terms of the other elastic stiffness coefficients.

Rigorous bounds for elastic stiffnesses for all crystal symmetries have been given by Mouhat and Coudert (2014) and for TI media with application to shales by Holt (2016). They follow from the requirement that the elastic strain energy density be positive, since otherwise the medium would be unstable (Nye 1985). These bounds tend to be too widely separated to provide a useful estimate of C_{13}, however. Because of this several authors have attempted to provide phenomenological constraints on C_{13}. Examples include the work of Yan et al. (2016), Chichinina and Vernik (2018) and Yan and Vernik (2021) discussed later in this paper.

The purpose of this paper is to examine the underlying physical mechanisms that control the value of C_{13}. It applies several rock-physics-based models of shale anisotropy to clarify how C_{13} relates to shale microstructure and to deepen understanding of this important elastic parameter. The paper first discusses several simple estimates of C_{13} and then analyzes rigorous bounds and phenomenological constraints. It then explores the roles of clay mineral anisotropy, the anisotropic orientation distribution of clay particles, fine-scale layering, and bedding-parallel microcracks. Finally, it discusses the findings and highlights the main conclusions of the study.

2 Simple Estimates of C_{13}

The simplest model of shale anisotropy is ANNIE (Schoenberg et al. 1996) with elastic stiffness matrix C_{ij} given by:

$$C_{ij} = \begin{bmatrix} \lambda + 2\mu_H & \lambda & \lambda & 0 & 0 & 0 \\ \lambda & \lambda + 2\mu_H & \lambda & 0 & 0 & 0 \\ \lambda & \lambda & \lambda + 2\mu & 0 & 0 & 0 \\ 0 & 0 & 0 & \mu & 0 & 0 \\ 0 & 0 & 0 & 0 & \mu & 0 \\ 0 & 0 & 0 & 0 & 0 & \mu_H \end{bmatrix}. \tag{6}$$

This model was designed to have positive anellipticity as exhibited by many shales. For ANNIE the anellipticity parameter $\eta = (\epsilon - \delta)/(1 + 2\delta)$ of Alkhalifah and Tsvankin (1995) takes the value

$$\eta = \frac{(\mu_H - \mu)}{(\lambda + 2\mu)}, \tag{7}$$

which is positive since the horizontal shear modulus μ_H is greater than the vertical shear modulus μ for most shales. Since this is a three-parameter TI model it has two constraints on the set of five ordinarily independent TI parameters, namely (Schoenberg et al. 1996):

$$C_{13} = C_{33} - 2C_{55}, \tag{8}$$

and

$$C_{13} = C_{12} \equiv C_{11} - 2C_{66}. \tag{9}$$

These relations are exact for an isotropic medium. Figure 1 compares the values of C_{13} in the range from 0 to 50 GPa from the database of shale elastic stiffnesses compiled by Horne (2013) with the right hand side of equations 8 and 9. It is seen that $C_{33} - 2C_{55}$ tends to underestimate C_{13} while $C_{12} = C_{11} - 2C_{66}$ tends to overestimate C_{13}, as pointed out by Yan and Vernik (2021) for their compilation of data for TI hydrocarbon source rocks.

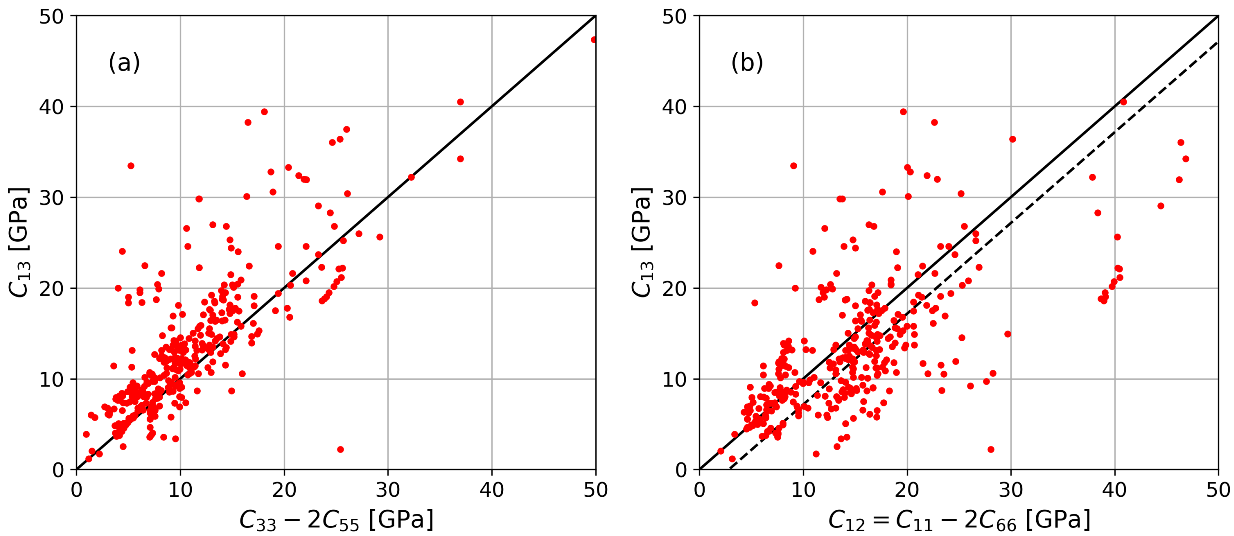

Figure 1: Comparison of C_{13} with (a) $C_{33} - 2C_{55}$ and (b) $C_{12} = C_{11} - 2C_{66}$ for the database of shale elastic stiffnesses in the range 0 to 50 GPa compiled by Horne (2013). ANNIE assumes these quantities are equal. The dashed line in (b) shows the relation (equation 11 in the text) with $\hat{M} - 2\hat{\mu} = 2.84$ GPa obtained by L1 inversion of the data.

Electron microscopy shows that clay platelets in shales vary in orientation but are locally aligned in domains (Swan et al. 1989; Hornby 1994; Schoenberg et al. 1996). Studies of illite by Aylmore and Quirk (1960) indicate that most porosity resides in very small pores (radius < 42 Å), interpreted as platelet separations of roughly 10–30 Å. Given that the in-plane dimensions of clay platelets are of ~ 700 Å, this supports a model of parallel crystals within domains, with minimal porosity between domains.

Since clay platelets are stiff compared with the medium lying between the platelets, a second model is an isotropic medium stiffened by the presence of stiff horizontally bedded thin plates following Schoenberg et al. (1996).

If λ and μ are the second-order Lamé elastic stiffnesses of the isotropic background medium and $\hat{M}$ and $\hat{\mu}$ are the excess normal and shear rigidity due to the presence of the thin platelets, the stiffness matrix of the plate-stiffened medium is:

$$C_{ij} = \begin{bmatrix} \lambda+2\mu+\hat{M} & \lambda+\hat{M}-2\hat{\mu} & \lambda & 0 & 0 & 0 \\ \lambda+\hat{M}-2\hat{\mu} & \lambda+2\mu+\hat{M} & \lambda & 0 & 0 & 0 \\ \lambda & \lambda & \lambda+2\mu & 0 & 0 & 0 \\ 0 & 0 & 0 & \mu & 0 & 0 \\ 0 & 0 & 0 & 0 & \mu & 0 \\ 0 & 0 & 0 & 0 & 0 & \mu+\hat{\mu} \end{bmatrix}. \tag{10}$$

(Schoenberg et al. 1996). This satisfies equation 8 together with:

$$C_{13} = C_{12} - \hat{M} + 2\hat{\mu}. \tag{11}$$

If $\hat{M} = 2\hat{\mu}$ then writing $\mu_H = \mu + \hat{\mu}$ gives the simple three parameter model ANNIE discussed earlier (see equation 6).

The dashed line in Figure 1(b) compares the right hand side of equation 11 with C_{13} from the database of shale elastic stiffnesses compiled by Horne (2013) in the range 0 to 50 GPa for a value $\hat{M} - 2\hat{\mu} = 2.84$ GPa obtained by L1 inversion of the data.

3 Rigorous Bounds for C_{13}

Rigorous bounds for elastic stiffnesses for all crystal symmetries have been given by Mouhat and Coudert (2014) and follow from the requirement that the elastic strain energy density W be positive, since otherwise the medium would be unstable (Nye 1985). In the Voigt two-index notation, W is given in terms of the elastic stiffnesses C_{ij} and strains ϵ_i by:

$$W = \frac{1}{2} C_{ij} \epsilon_i \epsilon_j, \tag{12}$$

where a sum over repeated indices is implied. As a result, C_{ij} is positive definite so that $W > 0$ for non-zero strain. For TI media, Mouhat and Coudert (2014) give the bounds as:

$$C_{11} > |C_{12}|,\ 2C_{13}^2 < C_{33}(C_{11} + C_{12}),\ C_{55} > 0,\ C_{66} > 0. \tag{13}$$

Holt (2016) wrote the bounds on C_{13} as:

$$-\sqrt{C_{33}(C_{11} - C_{66})} \le C_{13} \le \sqrt{C_{33}(C_{11} - C_{66})}. \tag{14}$$

Figure 2 compares C_{13} with the upper bound $C_{13}^{\max}$ and lower bound $C_{13}^{\min}$ for the database of shale elastic stiffnesses compiled by Horne (2013) for C_{13} in the range 0 to 50 GPa. It is seen that the upper bound for C_{13} is much closer to the measurements of C_{13} than is the lower bound. Nevertheless, the bounds appear to be too widely separated to provide useful estimates of C_{13}. Because of this several authors have attempted to provide phenomenological constraints on C_{13} and these are discussed next.

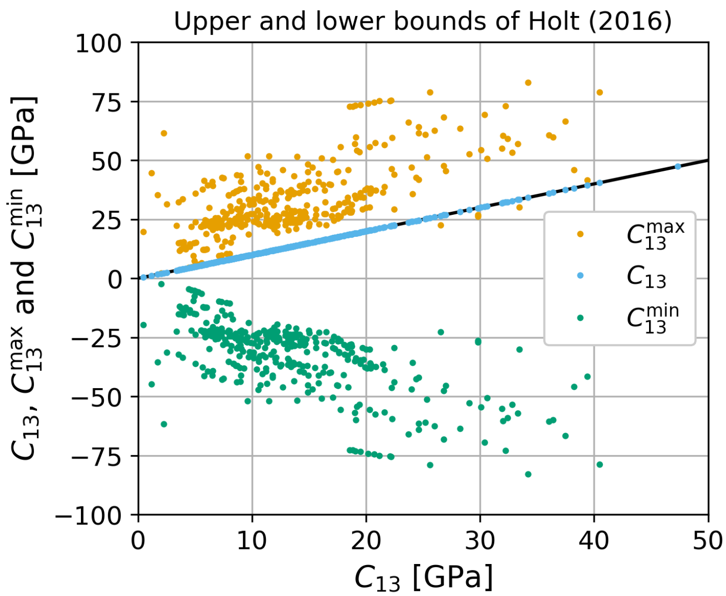

Figure 2: Comparison of C_{13} with its upper and lower bounds of Holt (2016) for the database of shale elastic stiffnesses compiled by Horne (2013) and C13 in the range 0 to 50 GPa.

4 Phenomenological Constraints on C_{13}

Yan et al. (2016) attempted to provide tighter upper and lower constraints on C_{13} based on their physical intuition that $\nu_{12} > 0$ and that $\nu_{13} > \nu_{12}$, where ν_{ij} is Poisson's ratio corresponding to a stress applied along axis x_i and strain measured along axis x_j. The first of these inequalities gives the upper constraint of Yan et al. (2016), while the second gives the lower constraint on C_{13} as follows:

$$\sqrt{C_{33}C_{12} + C_{66}^2} - C_{66} < C_{13} < \sqrt{C_{33}C_{12}}. \tag{15}$$

These constraints are compared with C_{13} based on the data of Horne (2013) in Figure 3 . It is seen that these phenomenological constraints are much closer to the measured values than are the rigorous bounds of Mouhat and Coudert (2014) and Holt (2016).

Yan et al. (2016) argued that data lying outside these constraints are less reliable and are "primarily caused by substantial uncertainty associated with the oblique velocity measurement". Sarout (2017), however, provided a counterexample to the assertion that $\nu_{13} > \nu_{12}$. This is based on the results of Postma (1955) for the long wavelength elastic properties of layered media consisting of two isotropic elastic media. For this counterexample $\nu_{13} < \nu_{12}$ thereby demonstrating that the lower phenomenological constraint of Yan et al. (2016) is not generally applicable to TI media and should not, therefore be used to filter elastic anisotropy data published in the literature.

Chichinina and Vernik (2018) proposed a phenomenological upper constraint for C_{13} corresponding to $\delta = \epsilon$, where ϵ and δ are Thomsen's anisotropy parameters, while maintaining the lower phenomenological constraint of Yan et al. (2016). This upper bound corresponds to elliptical anisotropy and is given by Chichinina and Vernik (2018) as:

$$C_{13}^{\max} = \sqrt{(C_{11} - C_{55})(C_{33} - C_{55})} - C_{55}. \tag{16}$$

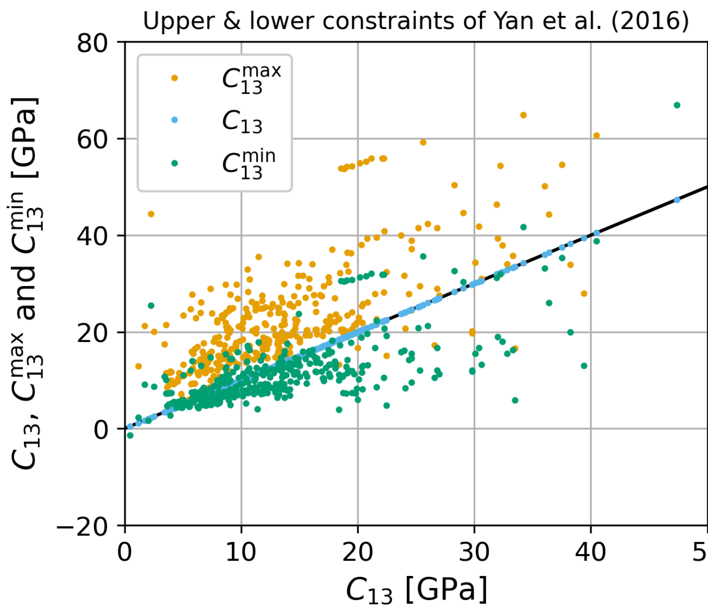

Figure 3: Comparison of C_{13} with the upper and lower constraints of Yan et al. (2016) for the database of shale elastic stiffnesses compiled by Horne (2013) and C_{13} in the range 0 to 50 GPa.

This is plotted together with the lower constraint of Yan et al. (2016) in Figure 4. Comparing with Figure 3 shows that the upper constraint of Chichinina and Vernik (2018) lies closer to the data than that of Yan et al. (2016).

Finally, Yan and Vernik (2021) noted in their compilation of data for TI hydrocarbon source rocks that $C_{33} - 2C_{55}$ tends to underestimate C_{13} while $C_{11} - 2C_{66}$ tends to overestimate C_{13} as seen also in Figure 1 for the anisotropy data compiled by Horne (2013). Based on this observation, Yan and Vernik (2021) propose the following phenomenological constraints on C_{13}:

$$C_{33} - 2C_{55} \leq C_{13} \leq C_{12} = C_{11} - 2C_{66}. \tag{17}$$

Concerning the lower phenomenological constraint, it is useful to rewrite the expression for Thomsen's δ in equation 1 as:

$$\delta = \chi + \frac{\chi^2}{2(1 - C_{55}/C_{33})}, \tag{18}$$

where

$$\chi = \frac{(C_{13} + 2C_{55} - C_{33})}{C_{33}}. \tag{19}$$

The lower phenomenological constraint corresponds to $\chi \geq 0$ and, therefore, to $\delta \geq 0$. The possibility of negative δ and, therefore, violation of the lower phenomenological constraint of Yan and Vernik (2021) is demonstrated, for example, by the results of walkaway VSP measurements (e.g. Leaney (1994)) which, in flat-lying sediments, give a local measurement of P- and S-phase slowness at many more angles than the three normally used in laboratory measurements.

It is clear from Figure 1 that the phenomenological constraints of Yan and Vernik (2021) are not rigorous bounds on C_{13}. Because of the relative closeness of the upper and lower phenomenological constraints of Yan and Vernik (2021), however, these authors suggested that an average of

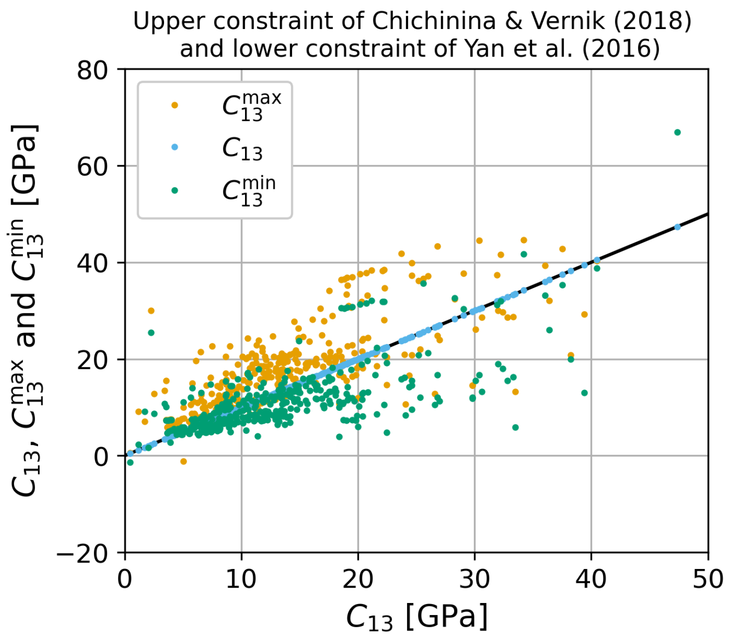

Figure 4: Comparison of C_{13} with the upper constraint of Chichinina and Vernik (2018) and lower constraint of Yan et al. (2016) for the database of shale elastic stiffnesses compiled by Horne (2013) and C_{13} in the range 0 to 50 GPa.

these constraints may offer a reasonable estimate of C_{13}. Figure 5 shows that while this average provides an estimate of C_{13}, there is still significant scatter.

To conclude this section note that though the phenomenological constraints discussed in this section may be used to estimate C_{13}, they do not provide information on how shale microstructure affects C_{13}. This is investigated in the following sections.

5 Anisotropy of Clay Minerals

Experimental measurements of single-crystal elastic moduli for clay minerals are unavailable due to their extremely small grain size (Katahara 1996). However, the complete elastic stiffness tensors for several dry clays and micas including kaolinite, illite-smectite and muscovite have been obtained from first-principles calculations by Militzer et al. (2011). Illite is compositionally and structurally similar to muscovite, for which elastic moduli have been experimentally measured. Table 1 compares experimental measurements of the elastic stiffnesses of muscovite by Vaughan and Guggenheim (1986) with the best-fitting TI media obtained by Sayers and Den Boer (2016) using the first-principles calculations for muscovite, illite-smectite and kaolinite by Militzer et al. (2011).

It is seen in Table 1 that $C_{13} \leq C_{12} = C_{11} - 2C_{66}$ for Muscovite, Illite-Smectite, Ideal Kaolinite and Kaolinite 2M*, consistent with the upper phenomenological constraint of Yan and Vernik (2021). Thus the violation of the upper constraint of Yan and Vernik (2021) by several points shown in Figure 1(a) cannot be explained by the properties of clay minerals alone. The lower constraint $C_{13} \geq C_{33} - 2C_{55}$ is seen to be violated by Ideal Kaolinite and Kaolinite 2M* that also

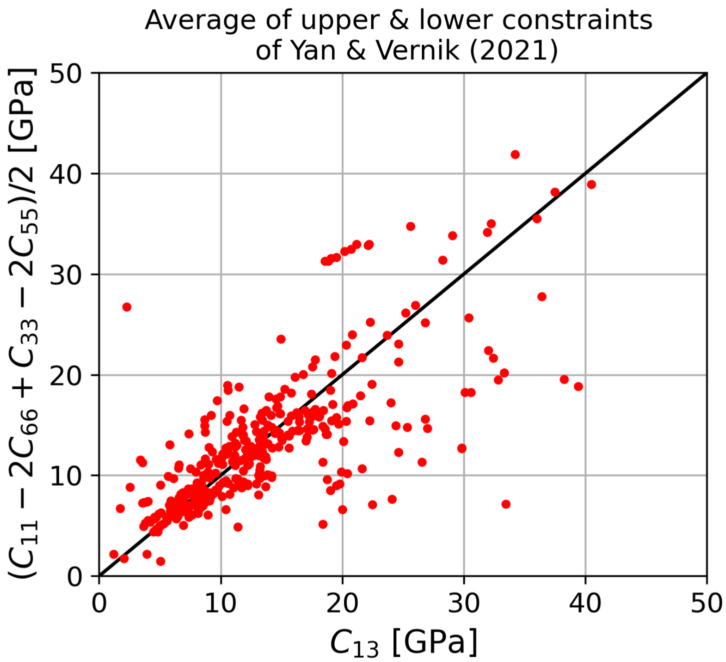

Figure 5: Comparison of C_{13} with the average of the upper and lower constraints of Yan and Vernik (2021).

Table 1: Comparison of elastic stiffnesses and anisotropy parameters for the best-fitting TI medium of Sayers and Den Boer (2016) derived from first-principle calculations of Militzer et al. (2011) for dry muscovite, illite-smectite and kaolinite, with the experimental measurements of elastic stiffnesses for muscovite measured by Vaughan and Guggenheim (1986)

.

Elastic Stiffness [GPa]	Muscovite	Illite-Smectite	Ideal Kaolinite	Kaolinite 2M*	Muscovite (measured)
$C_{11} = C_{22}$	181.3	171.8	185.9	186.1	179.7
C_{33}	60.1	25.2	83.7	82.5	58.6
$C_{44} = C_{55}$	20.3	11.5	14.8	14.7	18.0
C_{66}	66.3	68.1	58.8	59.1	72.0
$C_{13} = C_{23}$	24.8	4.1	5.3	5.9	23.4
$C_{12} = C_{11} - 2C_{66}$	48.8	35.6	68.2	67.8	48.8
$C_{33} - 2C_{55}$	19.5	2.2	54.1	53.1	22.6
ϵ	1.008	2.909	0.611	0.628	1.033
γ	1.133	2.461	1.487	1.510	1.500
δ	0.094	0.081	-0.377	-0.373	0.014

exhibit negative values of δ.

It should be noted that while electron microscopy shows that clay platelets in shales are locally aligned in domains, with compliant regions lying between the clay particles, the domains vary in orientation from place to place (Swan et al. 1989; Hornby 1994; Schoenberg et al. 1996). The effect of this on C_{13} is investigated in the next section.

6 Elastic Properties of Clay in Shales

Studies of illite by Aylmore and Quirk (1960) indicate that most porosity resides in very small pores (radius < 42 Å), interpreted as platelet separations of roughly 10–30 Å. Given that the in-plane dimensions of clay platelets are of ~700 Å, this supports a model of parallel crystals within domains, with minimal porosity between domains.

Because of the separation between clay platelets, and the presence of clay-bound water on their surfaces, the elastic stiffnesses of a domain are expected to be considerably lower than those of the clay mineral. This interpretation is supported by the measurements of Ulm and Abousleiman (2006) and Ortega et al. (2007), who combined ultrasonic velocity measurements with nano- and micro-indentation tests to infer the elastic properties of the clay matrix at length scales ranging from a few hundred to several thousand nanometers. By calibrating indentation-derived properties with ultrasonic velocity measurements, Ulm and Abousleiman (2006) and Ortega et al. (2007) found that the clay matrix can be described as a transversely isotropic (TI) medium with elastic stiffnesses that are significantly lower than the single crystal elastic stiffnesses listed in Table 1. This occurs because the regions between clay platelets are significantly more compliant than the clay platelets themselves.

Sayers and den Boer (2020) modeled a shale domain as aligned anisotropic clay platelets embedded in a compliant interparticle medium with properties representing the effect of clay-bound water and interparticle contacts. The resulting elastic stiffness coefficients depend on the anisotropy, aspect ratio, and volume fraction of the platelets, as well as the bulk and shear moduli of the interplatelet medium, assumed isotropic. Variations in clay anisotropy were explored by systematically varying these model parameters and examining their impact on the effective transversely isotropic (TI) stiffness tensor. Statistical analysis of the resulting distributions, and correlations among stiffnesses and anisotropy parameters, enables identification of the most probable stiffness sets for rock physics applications. Despite the use of random sampling, robust relationships between elastic stiffnesses emerge, consistent with trends reported for shales in the literature. As an example, taking the elastic stiffness C_{33} of the domain as the mode (12.5 GPa) of the distribution obtained, Sayers and den Boer (2020) obtained the following estimates of the remaining elastic constants: $C_{11} = C_{22} = 22.18$ GPa, $C_{44} = C_{55} = 3.74$ GPa, $C_{66} = 8.31$ GPa, $C_{12} = 5.55$ GPa, and $C_{13} = C_{23} = 5.53$ GPa. Thus $C_{13} < C_{12}$ and $C_{13} > C_{33} - 2C_{55}$, consistent with both phenomenological constraints of Yan and Vernik (2021).

It should be noted, however, that while clay platelets tend to be locally aligned in domains, the orientation of domains varies from place to place and the effect of this is discussed in the following section.

7 Effect of the Orientation Distribution of Clay Domains

Clay typically exhibits an anisotropic distribution of domain orientations. Within the Voigt approximation, the effective elastic stiffness tensor may be obtained by orientational averaging of the stiffness tensors of the domains (Sayers 1986, 1994). In contrast, the Reuss approximation yields the effective elastic compliance tensor through the corresponding orientational average of the domain compliance tensors (Sayers 1987). When both the domains and clay-platelet orientation distribution exhibit transversely isotropic symmetry, the elastic stiffness tensor is characterized by two orientation parameters, W_{200} and W_{400}, which arise in an expansion of the orientation distribution function in terms of generalized Legendre functions (Roe 1965; Morris 1969).

Figure 6 and Figure 7 show the predicted values of $C_{12} - C_{13}$ and $C_{13} - C_{33} + 2C_{55}$ as a function of W_{200} and W_{400} in the Voigt and Reuss approximations respectively using the elastic stiffnesses of the domain given above. Violation of the upper phenomenological constraint of Yan and Vernik (2021) occurs when $C_{12} - C_{13} < 0$, while violation of the lower phenomenological constraint of Yan and Vernik (2021) occurs when $C_{13} - C_{33} + 2C_{55} < 0$. It is seen in figures 6 and 7 that the upper constraint is violated if W_{200} is significantly larger than W_{400}, while the lower constraint is violated if W_{400} is significantly larger than W_{200}. Thus the orientation distribution of clay platelets is significant in determining the value of C_{13} and may be studied using X-ray or neutron diffraction.

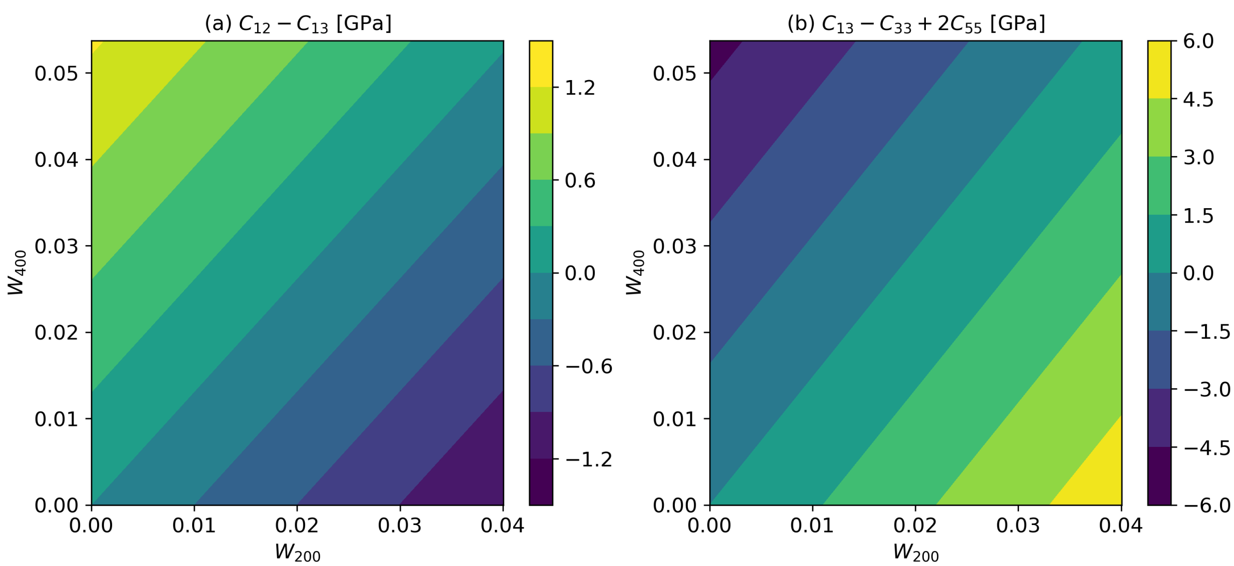

Figure 6: Predicted values of $C_{12} - C_{13}$ and $C_{13} - C_{33} + 2C_{55}$ as a function of W_{200} and W_{400} in the Voigt approximation for TI domains with elastic stiffnesses C_{11} = 22.18 GPa, C_{33} = 12.5 GPa, C_{55} = 3.74 GPa, C_{66} = 8.31 GPa, and C_{13} = 5.53 GPa. Violation of the upper phenomenological constraint of Yan and Vernik (2021) occurs when $C_{12} - C_{13} < 0$, while violation of the lower phenomenological constraint of Yan and Vernik (2021) occurs when $C_{13} - C_{33} + 2C_{55} < 0$.

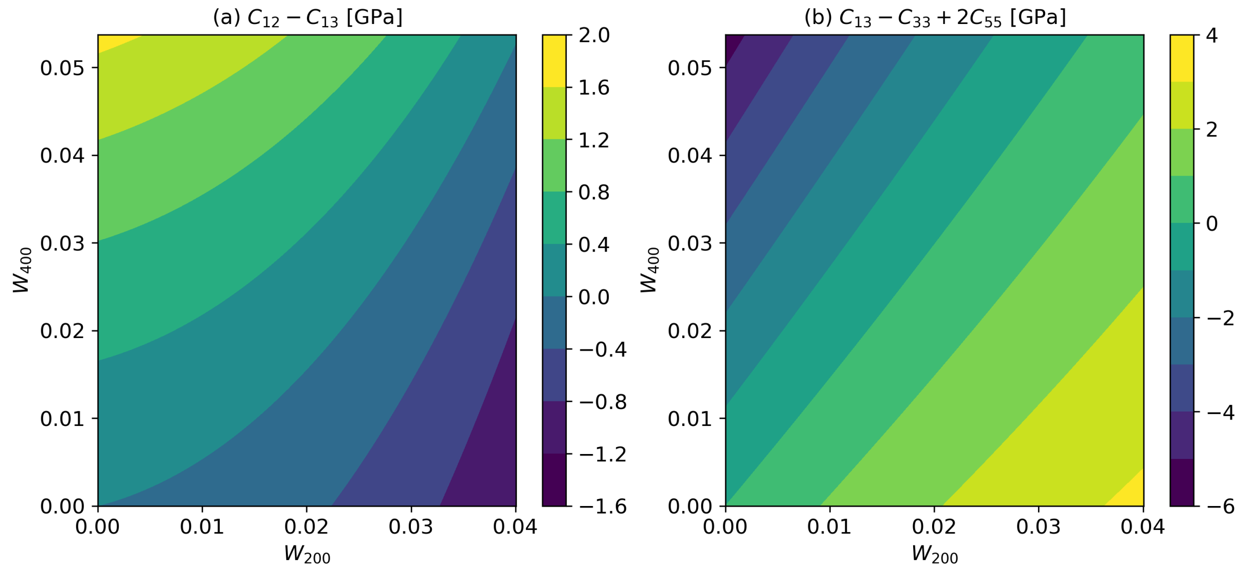

Figure 7: Predicted values of $C_{12} - C_{13}$ and $C_{13} - C_{33} + 2C_{55}$ as a function of W_{200} and W_{400} in the Reuss approximation for TI domains with elastic stiffnesses C_{11} = 22.18 GPa, C_{33} = 12.5 GPa, C_{55} = 3.74 GPa, C_{66} = 8.31 GPa, and C_{13} = 5.53 GPa. Violation of the upper phenomenological constraint of Yan and Vernik (2021) occurs when $C_{12} - C_{13} < 0$, while violation of the lower phenomenological constraint of Yan and Vernik (2021) occurs when $C_{13} - C_{33} + 2C_{55} < 0$.

8 Anisotropy due to Thin Layering

Since layering on a length scale smaller than the seismic wavelength frequently occurs in shale containing intervals, it is of interest to examine the effect of thin layering on C_{13}. For isotropic thin layers a simple example is the class of TI media referred to as K-media (Krey and Helbig 1956). Such media are equivalent in the long wavelength limit to stacks of layers having the same value of $\zeta = V_\mathrm{S}^2/V_\mathrm{P}^2 = \mu/(\lambda + 2\mu)$, where V_P and V_S are the P- and S-velocities in a layer, and λ and μ are the corresponding Lamé elastic stiffnesses. In the long wavelength limit such media are transversely isotropic with $C_{55}/C_{33} = \zeta$ and satisfy $C_{13} - C_{33} + 2C_{55} = 0$. Thus C_{13} for K-media coincide with the lower constraint of Yan and Vernik (2021). In addition, C_{13} is related to the other C_{ij} via the relation (Krey and Helbig 1956; Schoenberg et al. 1996).

$$C_{12} = C_{13}\frac{(C_{11} + C_{13})}{(C_{33} + C_{13})}. \tag{20}$$

Since $C_{33} < C_{11}$ for shales, the upper phenomenological constraint of Yan and Vernik (2021) is satisfied.

More generally, the five independent non-vanishing elastic stiffnesses for a medium composed of thin horizontal isotropic layers with Lamé elastic stiffnesses λ and μ are (Backus 1962; Helbig and Schoenberg 1987):

$$C_{11} = 4C_{66} - 4\langle\zeta\mu\rangle + C_{13}^2/C_{33}, \tag{21}$$

$$C_{33} = \langle\zeta\mu^{-1}\rangle^{-1}, \tag{22}$$

$$C_{55} = \langle\mu^{-1}\rangle^{-1}, \tag{23}$$

$$C_{66} = \langle \mu \rangle, \tag{24}$$

$$C_{13} = (1 - 2\langle \zeta \rangle) C_{33}, \tag{25}$$

where $\langle\rangle$ indicates averaging over layers.

Figure 8, Figure 9 and Figure 10 show the predictions of these equations for C_{13}, C_{12} and $C_{33} - 2C_{55}$ for three models comprising alternating sand and shale layers, with shale volume fraction denoted by c.

The elastic moduli of the sand and shale layers were selected according to the classification scheme of Rutherford and Williams (1989) for the AVO response of gas sands. In this scheme, class 1 gas sands have a higher normal-incidence acoustic impedance than the shale, class 2 sands have approximately the same acoustic impedance as the shale, and class 3 sands have a lower acoustic impedance than the shale. The elastic moduli used for the sand and shale layers were taken as those in models 1, 2, and 3 of Kim et al. (1993). The corresponding parameters are summarized in Table 2.

Table 2: Isotropic P- and S-velocities V_P and V_S, and density ρ for models 1, 2 and 3 of Kim et al. (1993)

.

Parameter	Model 1		Model 2		Model 3	
	shale	sand	shale	sand	shale	sand
V_P (km s^{-1})	3.30	4.20	2.96	3.49	2.73	2.02
V_S (km s^{-1})	1.70	2.70	1.38	2.29	1.24	1.23
ρ (g cm^{-3})	2.35	2.49	2.43	2.14	2.35	2.13

Model 1 corresponds to the Class 1 example of Rutherford and Williams (1989), derived from the Pennsylvanian Hartshorn Formation in the Arkoma Basin. For Model 2, shale properties were obtained by Kim et al. (1993), based on lower Pliocene to upper Miocene sediments from offshore Louisiana. The sand properties in this model were selected to yield a zero-offset reflectivity of 0.02 for a configuration in which shale overlies sand. Model 3 is based on data obtained from a blocked log of upper Pliocene delta-front sediments, also from offshore Louisiana (Kim et al. (1993)).

It is seen from figures 8 and 9 that for models 1 and 2, $C_{12} < C_{13} \leq C_{33} - 2C_{55}$. Thus for these models C_{13} is greater than C_{12} violating the upper phenomenological constraint of Yan and Vernik (2021) and the lower phenomenological constraint of Yan and Vernik (2021) is higher than their upper phenomenological constraint. Only for model 3 is the inequality $C_{33} - 2C_{55} < C_{13} < C_{12}$ satisfied as seen in figure 10. It follows also that Thomsen's anisotropy δ is negative for models 1 and 2 since C_{13} is lower than $C_{33} - 2C_{55}$ for these models, while δ is positive for model 3 as shown in Figure 11 , Figure 12 and Figure 13.

9 Anisotropy due to Bedding-parallel Microcracks

For a general transversely isotropic orientation distribution of microcracks, equations 16 – 21 of Sayers and Kachanov (1995) give the excess compliance tensor S_{ijkl} due to the presence of

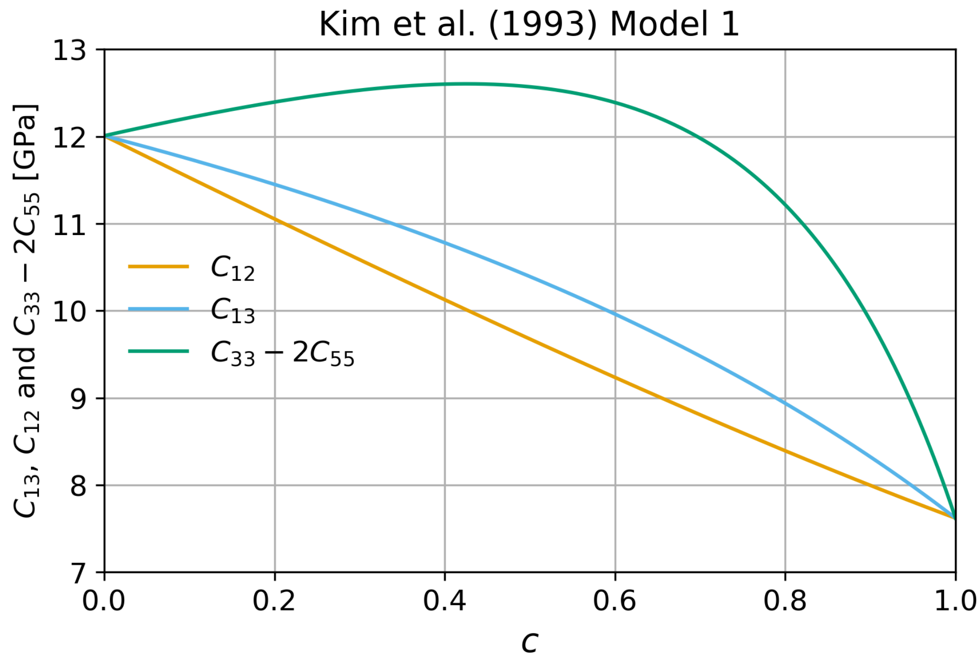

Figure 8: Predicted values of C_{13}, C_{12} and $C_{33} - 2C_{55}$ with shale volume fraction c using the properties of sand and shale for model 1 of Kim et al. (1993) in Table 2.

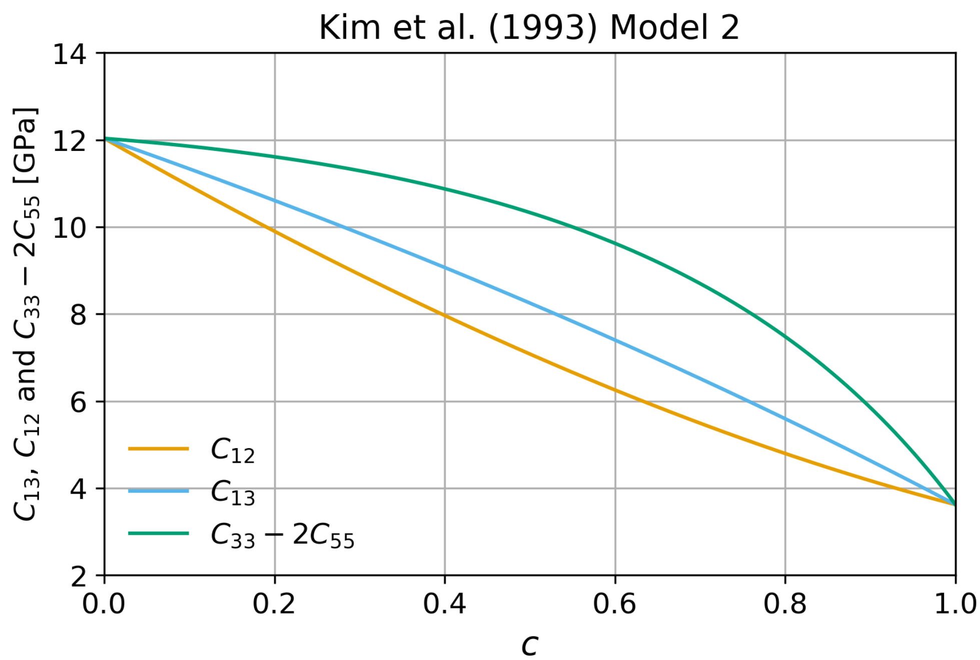

Figure 9: Predicted values of C_{13}, C_{12} and $C_{33} - 2C_{55}$ with shale volume fraction c using the properties of sand and shale for model 2 of Kim et al. (1993) in Table 2.

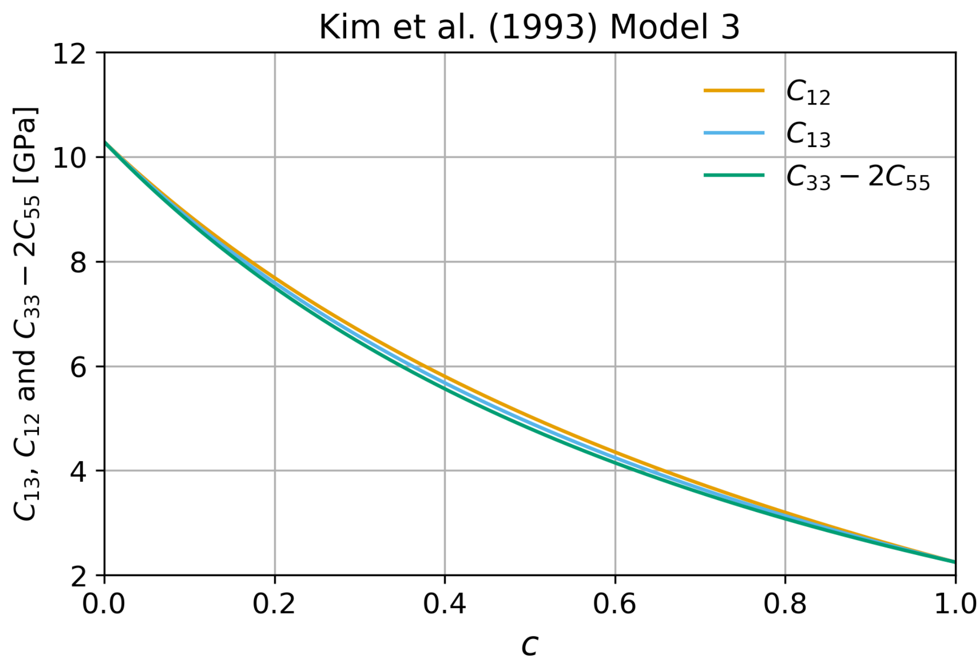

Figure 10: Predicted values of C_{13}, C_{12} and $C_{33} - 2C_{55}$ with shale volume fraction c using the properties of sand and shale for model 3 of Kim et al. (1993) in Table 2.

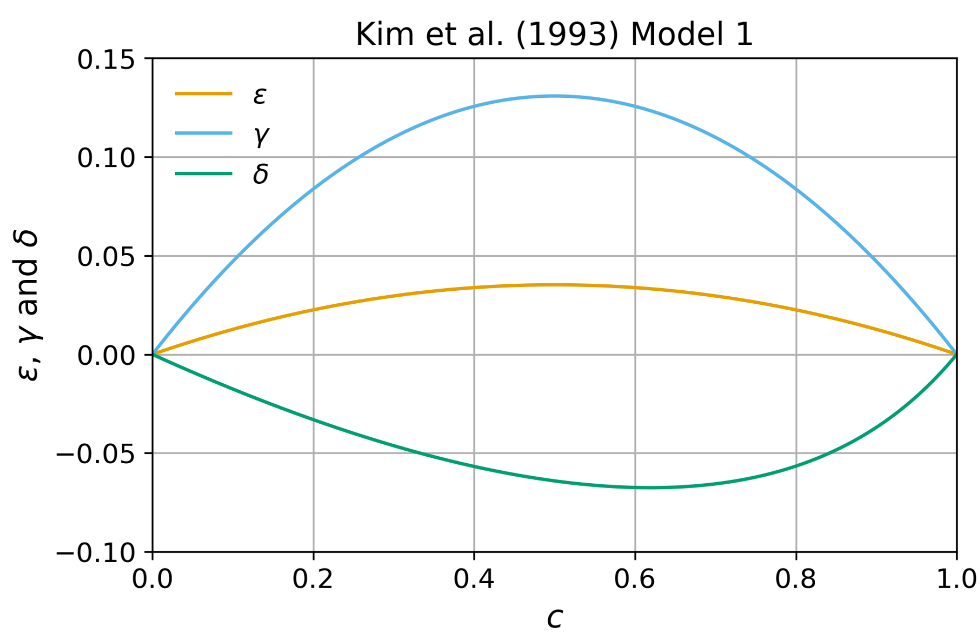

Figure 11: Predicted values of Thomsen's anisotropy parameters ϵ, γ and δ with shale volume fraction c using the properties of sand and shale for model 1 of Kim et al. (1993) in Table 2.

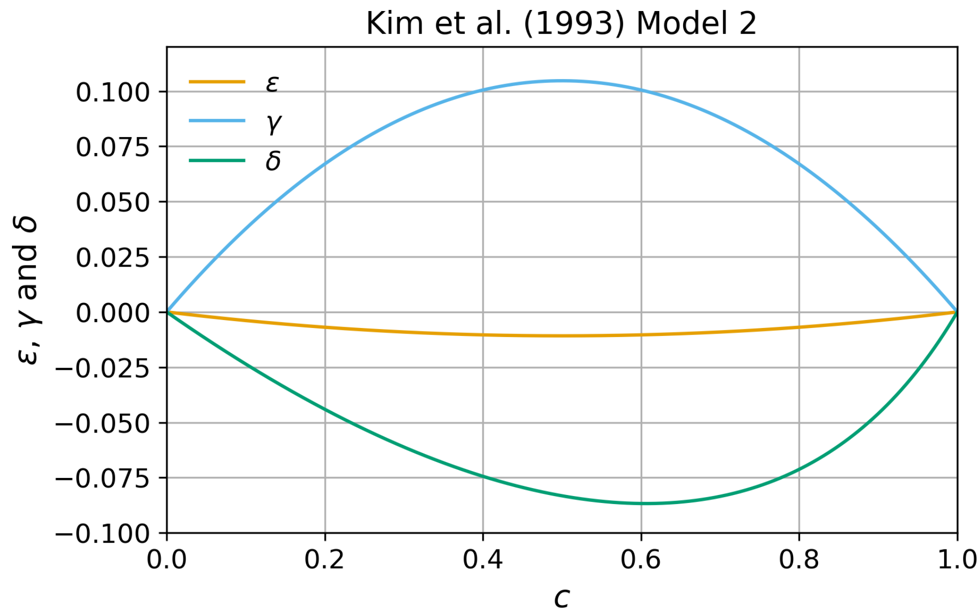

Figure 12: Predicted values of Thomsen's anisotropy parameters ϵ, γ and δ with shale volume fraction c using the properties of sand and shale for model 2 of Kim et al. (1993) in Table 2.

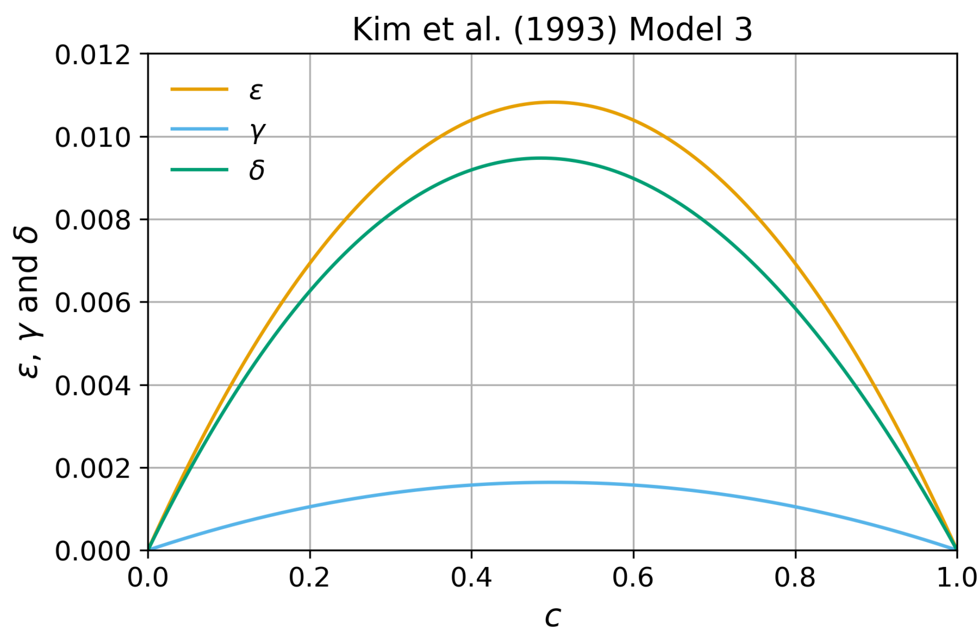

Figure 13: Predicted values of Thomsen's anisotropy parameters ϵ, γ and δ with shale volume fraction c using the properties of sand and shale for model 3 of Kim et al. (1993) in Table 2.

microcracks in terms of the components of the second and fourth rank tensors α_{ij} and β_{ijkl} defined by Kachanov (1992) as:

$$\alpha_{ij} = \frac{1}{V}\sum_{r=1}^{N} B_T^{(r)} n_i^{(r)} n_j^{(r)} A^{(r)}, \tag{26}$$

$$\beta_{ijkl} = \frac{1}{V}\sum_{r=1}^{N} (B_N^{(r)} - B_T^{(r)}) n_i^{(r)} n_j^{(r)} n_k^{(r)} n_l^{(r)} A^{(r)}. \tag{27}$$

The sum is over the N microcracks in volume V, and $B_N^{(r)}$ and $B_T^{(r)}$ are the normal and shear compliance of the r-th microcrack. The quantity $A^{(r)}$ is the area of the r-th crack, while $n_i^{(r)}$ is the ith component of the unit vector $\mathbf{n}$ normal to its surface. The elastic stiffness tensor C_{ijkl} may be obtained from the inverse of the elastic compliance tensor S_{ijkl} given by:

$$S_{ijkl} = S_{ijkl}^{(0)} + \Delta S_{ijkl}. \tag{28}$$

The quantity $S_{ijkl}^{(0)}$ is the elastic compliance tensor of the rock in the absence of microcracks.

For the case of bedding-parallel microcracks with coordinate axis x_3 perpendicular to bedding the normals to the microcracks have Cartesian components $n_1 = n_2 = 0,\ n_3 = 1$. For this case α_{33} and β_{3333} are non-zero and are given from equations 26 and 27 by

$$\alpha_{33} = \frac{1}{V}\sum_{r=1}^{N} B_T^{(r)} A^{(r)},\ \beta_{3333} = \frac{1}{V}\sum_{r=1}^{N} (B_N^{(r)} - B_T^{(r)}) A^{(r)}. \tag{29}$$

It is convenient to define quantities Z_N and Z_T by

$$Z_N = \frac{1}{V}\sum_{r=1}^{N} B_N^{(r)} A^{(r)},\ Z_T = \frac{1}{V}\sum_{r=1}^{N} B_T^{(r)} A^{(r)}. \tag{30}$$

This gives

$$\alpha_{33} = Z_T,\ \beta_{3333} = Z_N - Z_T. \tag{31}$$

If, in the two-index notation, C_{ij_b} are the elastic stiffnesses of the rock in the absence of microcracks, the TI elastic stiffnesses C_{ij} that result are:

$$C_{11} = \frac{\left[C_{11_b} + (C_{11_b}C_{33_b} - C_{13_b}^2)Z_N\right]}{1 + C_{33_b}Z_N}, \tag{32}$$

$$C_{33} = \frac{C_{33_b}}{1 + C_{33_b}Z_N}, \tag{33}$$

$$C_{55} = \frac{C_{55_b}}{1 + C_{55_b}Z_T}, \tag{34}$$

$$C_{66} = C_{66_b}, \tag{35}$$

$$C_{12} = \frac{C_{12_b} + (C_{33_b}C_{12_b} - C_{13_b}^2)Z_N}{1 + C_{33_b}Z_N}, \tag{36}$$

$$C_{13} = \frac{C_{13_b}}{1 + C_{33_b} Z_N}. \tag{37}$$

Hence

$$C_{12} - C_{13} = \frac{(C_{12_b} - C_{13_b}) + (C_{33_b} C_{12_b} - C_{13_b}^2) Z_N}{1 + C_{33_b} Z_N}, \tag{38}$$

$$C_{13} - C_{33} + 2C_{55} = \frac{(C_{13_b} - C_{33_b})}{1 + C_{33_b} Z_N} + \frac{2C_{55_b}}{1 + C_{55_b} Z_T}. \tag{39}$$

For shales that are isotropic in the absence of microcracks with

$$C_{11_b} = C_{33_b} = M,\ C_{55_b} = C_{66_b} = \mu,\ C_{12_b} = C_{13_b} = M - 2\mu, \tag{40}$$

the above become

$$C_{12} - C_{13} = \frac{2(M - 2\mu)\mu Z_N}{1 + M Z_N}, \tag{41}$$

$$C_{13} - C_{33} + 2C_{55} = \frac{2\mu(M Z_N - \mu Z_T)}{(1 + \mu Z_T)(1 + M Z_N)}. \tag{42}$$

Since Z_N and Z_T are positive it follows from equation 41 that $C_{12} > C_{13}$ if $\mu/M < 1/2$ and $C_{12} < C_{13}$ if $\mu/M > 1/2$. For the isotropic shales in Table 2, $\mu/M = 0.265$ for model 1, $\mu/M = 0.217$ for model 2 and $\mu/M = 0.206$ for model 3. Hence $C_{12} > C_{13}$ for all three models and the upper constraint of Yan and Vernik (2021) is satisfied.

From equation 42 it follows that $C_{13} > C_{33} - 2C_{55}$ if $Z_N/Z_T > \mu/M$ and $C_{13} < C_{33} - 2C_{55}$ if $Z_N/Z_T < \mu/M$. To gain insight into the expected magnitude of Z_N/Z_T , consider a simple model in which fluid-filled microcracks are represented as oblate spheroids of radius a and half-height c, such that the aspect ratio is given by c/a. In this framework, the normal-to-shear compliance ratio Z_N/Z_T may be estimated using the results of Hudson et al. (1996), who showed that for a random distribution of aligned fluid-filled isolated spheroids:

$$\frac{Z_N}{Z_T} = \frac{(1 - \nu/2)(1 + N)}{\left[1 + \frac{2a}{\pi c}\frac{K_f}{\mu}(1 - \nu)\right]}. \tag{43}$$

Quantities μ and ν are the shear modulus and the Poisson's ratio of the crack-free rock, K_f is the fluid bulk modulus and

$$N = \frac{4a}{\pi c}\left(\frac{i\omega\eta_f}{\mu}\right)\left(\frac{1 - \nu}{2 - \nu}\right). \tag{44}$$

The fluid viscosity is denoted by η_f , $i = \sqrt{-1}$, and ω is the angular frequency. The quantity N in equations 43 and 44 accounts for the effect of fluid viscosity on the response of the cracks to shear. It is seen that as the aspect ratio $c/a \to 0$, $Z_N/Z_T \to 0$ and C_{13} becomes less than $C_{33} - 2C_{55}$, thus violating the lower bound of Yan and Vernik (2021).

As an example of the combined effect of intrinsic anisotropy and microcrack anisotropy, consider the case of Greenhorn shale at 5000 ft depth (Jones and Wang 1981) for which C_{11} = 34.3 GPa, C_{33} = 22.7 GPa, C_{55} = 5.4 GPa, C_{66} = 10.6 GPa, C_{13} = 10.7 GPa and $C_{12} = C_{11} - 2C_{66} =$ 13.1 GPa. Figure 14 shows $C_{12} - C_{13}$ as a function of dimensionless normal compliance $C_{33_b} Z_N$ and $C_{13} - C_{33} + 2C_{55}$ for various values of Z_N/Z_T as a function of dimensionless shear compliance $C_{55_b} Z_T$. It is seen that the presence of microcracks leads to $C_{12} - C_{13}$ becoming increasingly positive. The quantity $C_{13} - C_{33} + 2C_{55}$ is negative for Greenhorn shale and becomes increasingly negative with increasing crack density if Z_N/Z_T is small. For larger values of Z_N/Z_T , however, $C_{13} - C_{33} + 2C_{55}$ becomes positive and increases in magnitude as crack density increases.

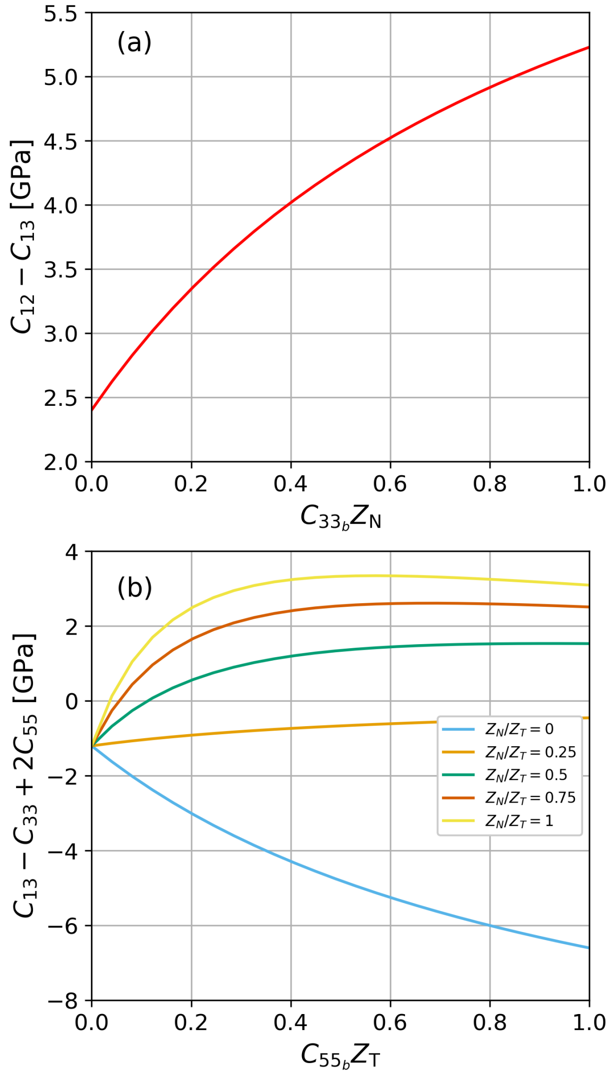

Figure 14: (a) $C_{12} - C_{13}$ as a function of dimensionless normal compliance $C_{33_b}Z_N$ and (b) $C_{13} - C_{33} + 2C_{55}$ for various values of Z_N/Z_T as a function of dimensionless shear compliance $C_{55_b}Z_T$ for Greenhorn Shale containing microcracks with normals parallel to the axis of rotational symmetry of the shale, assumed to be transversely isotropic.

10 Discussion and Conclusion

Many shales exhibit transverse isotropy (TI) with axis of rotational symmetry (x_3) oriented perpendicular to bedding with five independent elastic stiffness coefficients C_{11}, C_{33}, C_{55}, C_{66} and C_{13}. Elastic stiffness C_{13} is important for seismic velocity analysis, imaging, amplitude variation with offset (AVO) interpretation, and geomechanical applications, including wellbore stability, stress estimation, hydraulic fracture design, and reservoir compaction. However, determining C_{13} poses significant challenges because it requires measurements at oblique angles to the symmetry axis x_3, leading to increased uncertainty.

Because of this, several authors have attempted to constrain C_{13} using elastic stiffnesses obtained from velocity measurements for propagation parallel and perpendicular to the symmetry axis. In isotropic media, the relations $C_{13} = C_{12} = C_{11} - 2C_{66}$ and $C_{13} = C_{33} - 2C_{55}$ apply, but shale microstructure may break these equalities because of anisotropy due to preferred orientation of clay particles, fine-scale layering, and bedding-parallel microcracks. Based on their anisotropy database for hydrocarbon source rocks, Yan and Vernik (2021) proposed C_{12} and $C_{33} - 2C_{55}$ as upper and lower phenomenological constraints on C_{13}. However, these and other constraints do not address how shale microstructure influence C_{13}.

This paper examines the influence of clay mineral anisotropy, clay particle orientation distribution, fine-scale layering, and bedding-parallel microcracks on C_{13} to clarify the role of shale microstructure in governing this important parameter.

Single-crystal elastic stiffness coefficients computed from first principles for Muscovite and Illite-Smectite satisfy the constraints $C_{13} < C_{12} = C_{11} - 2C_{66}$ and $C_{13} > C_{33} - 2C_{55}$. While ideal Kaolinite and Kaolinite 2M* also satisfy the constraint $C_{13} < C_{12} = C_{11} - 2C_{66}$, they violate the constraint $C_{13} > C_{33} - 2C_{55}$, and exhibit a negative value of Thomsen's δ parameter.

The influence of an anisotropic orientation distribution of clay particles in shale on seismic anisotropy can be represented by the coefficients W_{200} and W_{400} in the expansion of the orientation distribution function using generalized Legendre functions. C_{13} may be greater than C_{12} if W_{200} is significantly larger than W_{400}, whereas C_{13} may be lower than $C_{33} - 2C_{55}$ if W_{200} is significantly smaller than W_{400}. This indicates that the orientation distribution of clay platelets plays an important role in determining the value of C_{13}.

Layering on length scales smaller than the seismic wavelength commonly occurs in sedimentary basins and can significantly influence C_{13}. Depending on layer properties, sand–shale layered formations with $C_{12} < C_{13} \leq C_{33} - 2C_{55}$ may occur.

Bedding-parallel microcracks typically increase $C_{12} - C_{13}$ and $C_{13} - C_{33} + 2C_{55}$, but $C_{13} - C_{33} + 2C_{55}$ may decrease if the ratio of normal-to-shear crack compliance is small, as expected for isolated fluid-filled cracks.

In conclusion, shale microstructure has an important effect on C_{13}, and the observations presented provide insight into its variability in shale formations.

References

T. Alkhalifah and I. Tsvankin. Velocity analysis for transversely isotropic media. *Geophysics*, 60 (5):1550–1566, 1995.

B. Amadei, W. Z. Savage, and H. S. Swolfs. Gravitational stresses in anisotropic rock masses. *International Journal of Rock Mechanics and Mining Sciences & Geomechanics Abstracts*, 24 (1):5–14, 1987.

L. A. G. Aylmore and J. P. Quirk. Domain or turbostratic structure of clays. *Nature*, 187(4742): 1046–1048, 1960.

G. E. Backus. Long-wave elastic anisotropy produced by horizontal layering. *Journal of Geophysical Research*, 67(11):4427–4440, 1962.

M. A. Biot and D. G. Willis. The elastic coefficients of the theory of consolidation. *Journal of Applied Mechanics*, 24:594–601, 1957.

T. Chichinina and L. Vernik. Physical bounds on c_{13} and δ for organic mudrocks. *Geophysics*, 83 (5):A75–A79, 2018.

K. Helbig and M. Schoenberg. Anomalous polarization of elastic waves in transversely isotropic media. *The Journal of the Acoustical Society of America*, 81(5):1235–1245, 1987.

R. M. Holt. Bounds of elastic parameters characterizing transversely isotropic media: Application to shales. *Geophysics*, 81(5):C243–C252, 2016.

B. E. Hornby. *The elastic properties of shales.* PhD thesis, University of Cambridge, 1994.

B. E. Hornby. Experimental laboratory determination of the dynamic elastic properties of wet, drained shales. *Journal of Geophysical Research: Solid Earth*, 103(B12):29945–29964, 1998.

S. A. Horne. A statistical review of mudrock elastic anisotropy. *Geophysical Prospecting*, 61(4): 817–826, 2013.

J. A. Hudson, E. Liu, and S. Crampin. The mechanical properties of materials with interconnected cracks and pores. *Geophysical Journal International*, 124(1):105–112, 1996.

L. E. A. Jones and H. F. Wang. Ultrasonic velocities in cretaceous shales from the Williston basin. *Geophysics*, 46(3):288–297, 1981.

M. Kachanov. Effective elastic properties of cracked solids: critical review of some basic concepts. *Applied Mechanics Reviews*, 45:304–335, 1992.

K. W. Katahara. Clay mineral elastic properties. In *SEG technical program expanded abstracts 1996*, pages 1691–1694. Society of Exploration Geophysicists, 1996.

K. Y. Kim, K. H. Wrolstad, and F. Aminzadeh. Effects of transverse isotropy on P-wave AVO for gas sands. *Geophysics*, 58(6):883–888, 1993.

T. Krey and K. Helbig. A theorem concerning anisotropy of stratified media and its significance for reflection seismics. *Geophysical Prospecting*, 4(3):294–302, 1956.

W. S. Leaney. Anisotropy and AVO from walkaways. In *SEG Technical Program Expanded Abstracts 1994*, pages 105–109. Society of Exploration Geophysicists, 1994.

B. Militzer, H.-R. Wenk, S. Stackhouse, and L. Stixrude. First-principles calculation of the elastic moduli of sheet silicates and their application to shale anisotropy. *American Mineralogist*, 96 (1):125–137, 2011.

P. R. Morris. Averaging fourth-rank tensors with weight functions. *Journal of Applied Physics*, 40 (2):447–448, 1969.

F. Mouhat and F.-X. Coudert. Necessary and sufficient elastic stability conditions in various crystal systems. *Physical Review B*, 90(22):224104, 2014.

J. F. Nye. *Physical properties of crystals: their representation by tensors and matrices*. Oxford University Press, 1985.

J. A. Ortega, F.-J. Ulm, and Y. Abousleiman. The effect of the nanogranular nature of shale on their poroelastic behavior. *Acta Geotechnica*, 2(3):155–182, 2007.

G. W. Postma. Wave propagation in a stratified medium. *Geophysics*, 20(4):780–806, 1955.

R.-J. Roe. Description of crystallite orientation in polycrystalline materials. III. General solution to pole figure inversion. *Journal of Applied Physics*, 36(6):2024–2031, 1965.

A. Rüger. P-wave reflection coefficients for transversely isotropic models with vertical and horizontal axis of symmetry. *Geophysics*, 62(3):713–722, 1997.

S. R. Rutherford and R. H. Williams. Amplitude-versus-offset variations in gas sands. *Geophysics*, 54(6):680–688, 1989.

J. Sarout. Comment on "Physical constraints on c_{13} and δ for transversely isotropic hydrocarbon source rocks" by F. Yan, D.-H. Han and Q. Yao. *Geophysical Prospecting*, 65(1):379–380, 2017.

C. M. Sayers. Angular dependent ultrasonic wave velocities in aggregates of hexagonal crystals. *Ultrasonics*, 24(5):289–291, 1986.

C. M. Sayers. The elastic anisotropy of polycrystalline aggregates of zirconium and its alloys. *Journal of Nuclear Materials*, 144(3):211–213, 1987.

C. M. Sayers. The elastic anisotropy of shales. *Journal of Geophysical Research: Solid Earth*, 99 (B1):767–774, 1994.

C. M. Sayers and L. D. Den Boer. The elastic anisotropy of clay minerals. *Geophysics*, 81(5): C193–C203, 2016.

C. M. Sayers and L. D. den Boer. Effect of variations in microstructure on clay elastic anisotropy. *Geophysics*, 85(2):MR73–MR82, 2020.

C. M. Sayers and M. Kachanov. Microcrack-induced elastic wave anisotropy of brittle rocks. *Journal of Geophysical Research: Solid Earth*, 100(B3):4149–4156, 1995.

M. Schoenberg, F. Muir, and C. Sayers. Introducing ANNIE: A simple three-parameter anisotropic velocity model for shales. *Journal of Seismic Exploration*, 5(1):35–49, 1996.

G. Swan, J. Cook, S. Bruce, and R. Meehan. Strain rate effects in Kimmeridge Bay Shale. *International Journal of Rock Mechanics and Mining Sciences & Geomechanics Abstracts*, 26(2): 135–149, 1989.

M. J. Thiercelin and R. A. Plumb. Core-based prediction of lithologic stress contrasts in East Texas formations. *SPE Formation Evaluation*, 9(04):251–258, 1994.

L. Thomsen. Weak elastic anisotropy. *Geophysics*, 51(10):1954–1966, 1986.

L. Thomsen. Weak anisotropic reflections. In J. P. Castagna and M. Backus, editors, *Offset-dependent reflectivity—Theory and practice of AVO analysis*, pages 103–111. Soc. Expl. Geophys, 1993.

F.-J. Ulm and Y. Abousleiman. The nanogranular nature of shale. *Acta Geotechnica*, 1(2):77–88, 2006.

M. T. Vaughan and S. Guggenheim. Elasticity of muscovite and its relationship to crystal structure. *Journal of Geophysical Research: Solid Earth*, 91(B5):4657–4664, 1986.

F. Yan and L. Vernik. Phenomenological models for estimating and constraining c_{13} for transversely isotropic hydrocarbon source rocks. *Geophysics*, 86(5):MR255–MR260, 2021.

F. Yan, D.-H. Han, and Q. Yao. Physical constraints on c_{13} and δ for transversely isotropic hydrocarbon source rocks. *Geophysical Prospecting*, 64(6):1524–1536, 2016.